Accurate and robust extraction of brain regions using a deformable model based on radial basis functions

Jia-Xiu Liu[a], Yong-Sheng Chen[a], Li-Fen Chen[b,c,*]

[a] Department of Computer Science, National Chiao Tung University, Hsinchu, Taiwan
[b] Institute of Brain Science, National Yang-Ming University, Taipei, Taiwan
[c] Department of Medical Research and Education, Taipei Veterans General Hospital, Taipei, Taiwan

ABSTRACT

Brain extraction from head magnetic resonance (MR) images is a classification problem of segmenting image volumes into brain and non-brain regions. It is a difficult task due to the convoluted brain surface and the inapparent brain/non-brain boundaries in images. This paper presents an automated, robust, and accurate brain extraction method which utilizes a new implicit deformable model to well represent brain contours and to segment brain regions from MR images. This model is described by a set of Wendland's radial basis functions (RBFs) and has the advantages of compact support property and low computational complexity. Driven by the internal force for imposing the smoothness constraint and the external force for considering the intensity contrast across boundaries, the deformable model of a brain contour can efficiently evolve from its initial state toward its target by iteratively updating the RBF locations. In the proposed method, brain contours are separately determined on 2D coronal and sagittal slices. The results from these two views are generally complementary and are thus integrated to obtain a complete 3D brain volume. The proposed method was compared to four existing methods, Brain Surface Extractor, Brain Extraction Tool, Hybrid Watershed Algorithm, and Model-based Level Set, by using two sets of MR images as well as manual segmentation results obtained from the Internet Brain Segmentation Repository. Our experimental results demonstrated that the proposed approach outperformed these four methods when jointly considering extraction accuracy and robustness.

© 2009 Elsevier B.V. All rights reserved.

1. Introduction

Brain extraction is essential or beneficial to many neuroimaging applications. For example, removal of the non-brain tissues facilitates the correction of intensity non-uniformity for magnetic resonance (MR) images (Acosta-Cabronero et al., 2008). Tissue segmentation algorithms for separating brain regions into grey matter (GM), white matter (WM), and cerebrospinal fluid (CSF) usually incorporate brain extraction as a preprocessing step to simplify the segmentation problem (Dale et al., 1999; Zhang et al., 2001; Shattuck et al., 2001). Extraction of brain regions can improve the accuracy of brain image registration by avoiding the interference of inter-subject variation of non-brain structures (Woods et al., 1998), including affine and non-rigid methods (Jenkinson and Smith, 2001; Gholipour et al., 2007; Liu et al., 2008a). In the past decade, voxel-based morphometry (VBM) (Ashburner and Friston, 2000)

has been extensively applied to statistically reveal regions with significant structural discrepancy between image groups (Good et al., 2001a, b; Beyer and Krishnan, 2002; Brenneis et al., 2003; Karas et al., 2003). Recent studies indicated that accurate brain extraction can improve the validity of VBM results because of better tissue segmentation and brain registration (Fein et al., 2006; Acosta-Cabronero et al., 2008).

Brain extraction algorithms can be classified into four major classes: (1) thresholding/clustering based methods, (2) boundary-based methods, (3) deformable model methods, and (4) hybrid methods. Thresholding/clustering based methods extract brain regions according to the phenomenon that intensities of the voxels belonging to the same tissue are similar. Lemieux et al. (1999) proposed a fine-tuned algorithm which utilizes several intensity thresholds and morphological operations to remove non-brain areas. Analysis of Functional NeuroImages (AFNI) fits a Gaussian mixture model to the intensity histogram of a brain image and estimates an intensity range to segment the brain areas in a slice-by-slice manner (Cox, 1996; Ward, 1999). Hahn and Peitgen (2000) presented a watershed algorithm which uses a connectivity criterion, pre-flooding height, to group image voxels with similar intensities and then regards the largest connected component as

the brain volume. More examples can be found in Brummer et al. (1993), Lee et al. (1998), Worth et al. (1998), Hata et al. (2000), Stokking et al. (2000), and Huh et al. (2002). Methods of this type are usually sensitive to image scanning parameters and image artifacts, such as noise and intensity inhomogeneity. Therefore, user intervention is usually required to determine proper parameters.

Boundary-based methods locate brain boundaries using the edge information obtained from image derivatives. Bomans et al. (1990) presented a semi-automated algorithm in which the brain region was manually labelled from the connected components detected with the Marr–Hildreth operator. Brain Surface Extractor (BSE) method improved the work of Bomans et al. (1990) by adaptively smoothing the noisy regions, detecting structure edges, and automatically determining the brain volume (Sandor and Leahy, 1997; Shattuck et al., 2001). In contrast to the thresholding/clustering based approaches, these methods are less sensitive to intensity inhomogeneity and scanning parameters. However, automated methods of this type may encounter difficulties in differentiating true boundaries from the false ones. For example, the GM/WM edges are usually very close to the target boundaries, the CSF/GM edges, and thus may perplex the determination of the brain volume.

Extraction methods using deformable models segment brain volumes by evolving contour or surface toward the target. Deformable model can be characterized by its representation method, implicit or explicit, and the evolution scheme (Xu et al., 2000; Montagnat et al., 2001). An explicit model directly describes the brain contour or surface and the fitting process is usually rapid (Davatzikos and Bryan, 1996; Kelemen et al., 1999; Dale et al., 1999; Smith, 2002). On the other hand, implicit model can easily change the model topology, for example, to split or merge objects, but the computational complexity is usually high. The level set method adopted in Zhuang et al. (2006) is an example of this kind of methods. Brain extraction using deformable model is generally more robust and accurate compared to the thresholding/clustering based and boundary-based methods (Smith, 2002; Ségonne et al., 2004; Zhuang et al., 2006). Moreover, incorporation of constraints or prior knowledge about the brain shape is relatively easy for this kind of methods. Therefore, they are more robust to both image artifacts and boundary discontinuities and can achieve subvoxel accuracy (Xu et al., 2000).

Hybrid approaches integrate the methods of different types with the anticipation to draw on the specific strengths at the expense of more computational cost (Atkins and Mackiewich, 1998; Aboutanos et al., 1999; Germond et al., 2000; Baillard et al., 2001; Rex et al., 2004; Mikheev et al., 2008). Ségonne et al. (2004) applied the watershed algorithm (Hahn and Peitgen, 2000) to generate an initial brain volume and incorporated the prior information of the brain shape into a deformable model to refine the extraction results. Rehm et al. (2004) integrated the extraction results obtained from atlas registration (Woods et al., 1998), intensity thresholding, and the BSE algorithm (Sandor and Leahy, 1997; Shattuck et al., 2001) by means of voting in the brain volume.

For large-scale studies, both accuracy and efficiency are important issues when considering brain extraction algorithms (Fennema-Notestine et al., 2006). The level set methods, which use implicit deformable models, are superior in accuracy and robustness, but the computational complexity of these methods is usually very high. On the contrary, methods using explicit models are generally more efficient. However, the discretization process in this kind of methods needs to compromise between the extraction accuracy and evolution efficiency. Finer (coarser) discretization employs more (fewer) sampling points to model object boundaries and can achieve more precise (rougher) results at a relatively slow (rapid) evolution speed.

In this work, we designed a new deformable model and developed an automated brain extraction method. The deformable model is implicitly represented by a set of Wendland's radial basis functions (RBFs) and can efficiently evolve toward the target boundary by iterative updates of RBF locations. Because of the use of RBFs, the new model can smoothly represent object boundaries though each RBF keeps a distance to the neighboring ones. Brain contours of 2D coronal and sagittal slices are individually fitted. The results of these two views are generally complementary and thus can be integrated to obtain accurate 3D brain volumes. According to our experiments, the proposed brain extraction method outperformed others when jointly considering extraction accuracy and robustness.

2. Methods

The proposed brain extraction method comprises three major steps, as shown in Fig. 1. Image intensity parameters and brain centroid are first estimated for the following segmentation procedures. Then the proposed deformable model is applied to extract the brain area on each of the coronal and sagittal slices. Complementary areas extracted from two different views are then integrated into a complete 3D brain volume.

2.1. Estimation of image intensity parameters and brain centroid

We estimate the effective intensity range and centroid of the head as the work of Smith (2002). An effective intensity range $[t_1, t_2]$ is determined to ignore the voxels with unusual intensities, such as noises or DC spikes, in which t_1 and t_2 are the intensity values in the histogram such that the accumulated number of voxels reaches 2% and 98%, respectively, as shown in Fig. 1. To roughly separate the head from the background, the threshold t is set to be 10% in the range of $[t_1, t_2]$. The brain centroid **O** is calculated by the first order image moment using the voxels with intensity value in the range of $[t, t_2]$.

An ellipsoid approximating the brain shape is determined by detecting the head bounding box from those voxels with intensity within $[t, t_2]$. The polar radius is set to the distance between the centroid and superior plane and the two equatorial radii are set to the halves of the distances between the opposite bounding planes, that is, the left-right and the anterior–posterior planes.

Difference of Gaussian (DOG) operator provides brain structure information which can be used for the detection of the mid-sagittal plane (MSP) of the brain (Liu et al., 2008b) and for the estimation of the brain tissue intensities. DOG performs image subtraction after the convolution with two Gaussian kernels $G(\sigma_1)$ and $G(\sigma_2)$, $\sigma_1 > \sigma_2$:

$$DOG(I, \sigma_1, \sigma_2) = G(\sigma_1) * I - G(\sigma_2) * I, \tag{1}$$

where I is a T1-weighted MR image and "$*$" denotes the convolution operator. The voxels with DOG values smaller than zero are in the regions with relatively high intensities, which are mostly the WM areas in the brain. Therefore, the median intensity of these voxels within the brain-approximating ellipsoid estimates the global WM intensity, t_w. On the other hand, the regions with DOG values larger than zero indicate the tissues with relatively low intensities. These voxels within the ellipsoid are mostly the GM and CSF. We apply Otsu's algorithm (Otsu, 1979) to calculate an intensity threshold t_o for separating CSF voxels from GM voxels. The median intensity of the CSF voxels estimates the global CSF intensity, t_c.

2.2. Brain extraction on the slices in two views

Brain extraction using deformable model generally requires a constraint to keep the contour or surface smooth. Loosening this
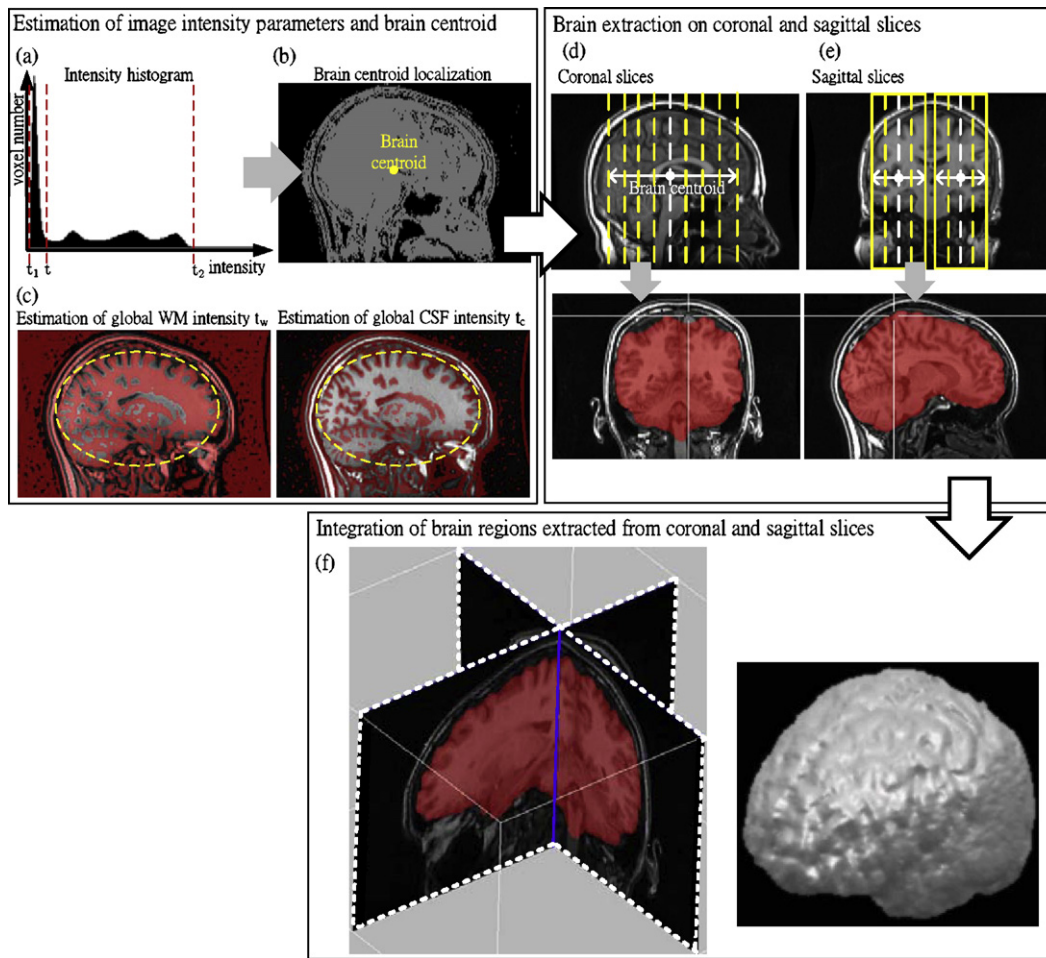
Fig. 1. Flowchart of the proposed method. (a) The effective intensity range $[t_1, t_2]$ and a rough head/background threshold t are estimated from the intensity histogram. (b) Then the voxels with intensity value within $[t, t_2]$ are used to approximate the brain centroid. (c) Applying DOG operator with zero threshold, the global WM intensity t_w and CSF intensity t_c are decided from the voxels within the ellipsoid approximating the brain shape. The brain areas of the (d) coronal slices and (e) sagittal slices are extracted. (f) A complete 3D brain region is determined from the complementary areas segmented from two different views.

constraint may lead to better fitting for the uneven brain surface but may face the risk of leakage through the weak boundaries. On the other hand, models with strict smoothness constraint can achieve stable results, but they usually underestimate the curvature of brain surface. To tackle this problem, Smith (2002) utilized a hyperbolic tangent function with empirically obtained maximum and minimum curvature values to adaptively smooth the model of brain surface.

In this work, we apply the deformable contour model to extract the brain regions on both coronal and sagittal slices and then integrate the results from two views. As shown in Fig. 2, local curvatures of a region extracted from different views are usually quite different. Fitting a local boundary in the view with relatively low curvatures often achieve more reliable results, whereas the boundaries frequently cut through the tissues due to the high curvatures in another view. Therefore, segmentation results in different views can complement each other. Applying a strict smoothness constraint for two views followed by the simple logical OR operation for the integration can achieve accurate and stable extraction. Notice that brain extraction on the axial slices is not considered in this work because of the efficiency issue.

The segmentation in the coronal view starts with the slice nearest to the brain centroid **O** and proceeds with the slices toward the anterior and posterior directions. The extraction on the sagittal slices, which are parallel to the detected MSP, is divided into two parts. Each part starts with a sagittal slice 30 mm apart from the MSP and proceeds with the slices toward the MSP and the most lateral slice, as shown in Fig. 1. Sagittal slices within 3 mm from the MSP are not processed to avoid the unstable segmentation due to relatively few GM and WM tissues. Because the extracted brain region shrinks gradually as the extraction goes forward along the anterior, posterior, left, and right directions, brain extraction in each of these directions is terminated once the size of the extracted brain region is smaller than a threshold.

2.3. Initial contour

An initial contour within the brain region is required for each of the three starting slices, as shown in Fig. 3. The brain bounding box is first detected from those pixels with their intensity values within $[t, t_2]$. In this way the lower boundary of the bounding box is usually located at the bottom of the MR volume and is thus adjusted according to the aspect ratios 8:7 and 4:3 for the coronal and sagittal slices, respectively. A set of Wendland's RBFs are then equally spread along an ellipse centered in the bounding box with the lengths of its axes set to be 0.7 times the length and width of the box. These RBFs determine an initial contour which can evolve to fit the brain contour by the method described in the next section. Because the brain contours of adjacent slices are usually similar, the evolved contour of current slice provides a good initial for the neighboring ones. This propagation way improves the performance of brain extraction, in terms of both accuracy and efficiency.
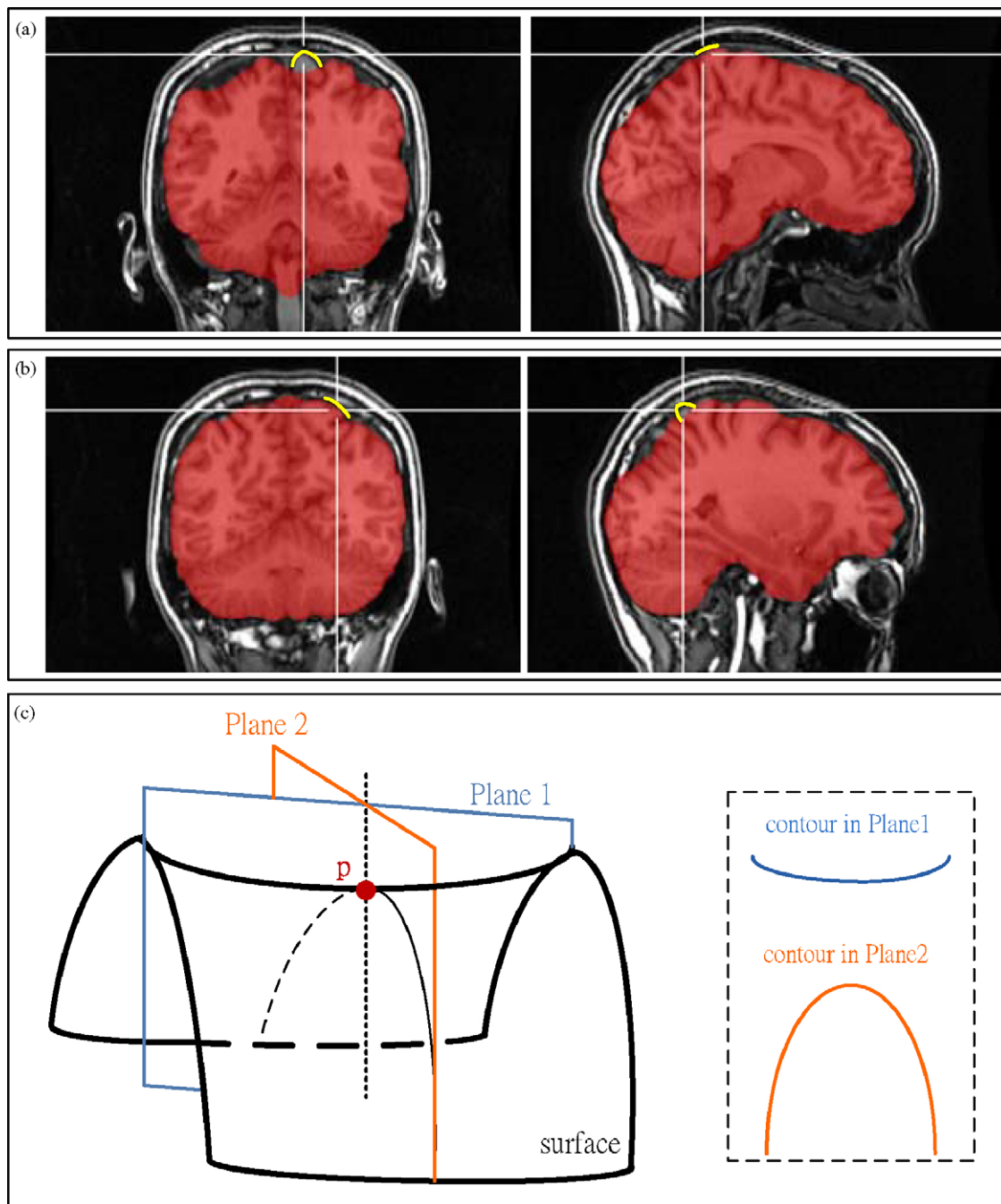
Fig. 2. Brain surface presentsquite different curvatures in the coronal and sagittal views. (a) The yellow curves show that the local curvature of brain surface in the coronal view is significantly higher than that in the sagittal view, and (b) vice versa. (c) Boundary fitting can achieve more reliable results with low curvatures than with high curvatures. The regions marked as red in (a) and (b) illustrate that the fitting results obtained from coronal and sagittal views are mutually complementary. (For interpretation of the references to colour in this figure legend, the reader is referred to the web version of the article.)
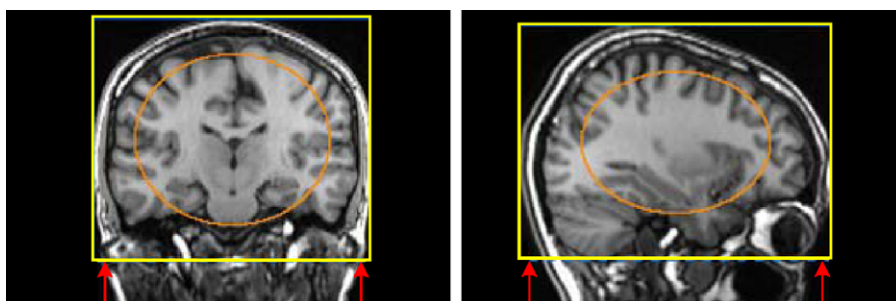
Fig. 3. An elliptic contour centered in the approximated bounding box of the brain is regarded as the initial contour for the brain extraction on each of the starting slices.
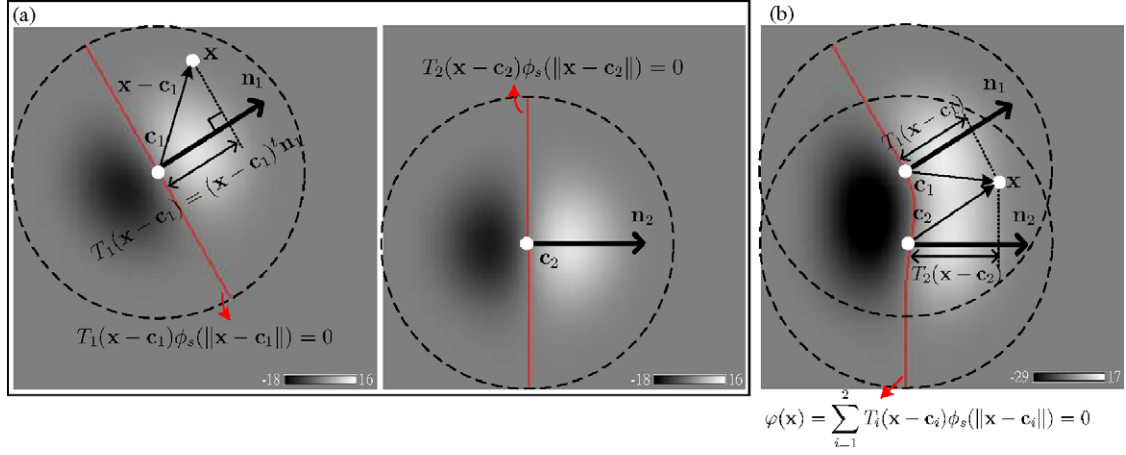
Fig. 4. Implicit contour representation. (a) Image intensity in this figure represents the value of $T_i(\cdot)\phi_s(\cdot)$. The zero set where $T_i(\cdot)\phi_s(\cdot) = 0$ within the compact support region represents the implicit model, marked as the red line. (b) The combination of $T_i(\cdot)\phi_s(\cdot)$ can represent contour smoothly. (For interpretation of the references to colour in this figure legend, the reader is referred to the web version of the article.)

2.4. Deformable model for brain extraction

2.4.1. Implicit contour representation

A contour in a d-dimensional image space (d is 2 or 3) can be implicitly modeled as the zero set of a scalar function $\varphi : \Re^d \to \Re$:

$$C = \{\mathbf{x}|\varphi(\mathbf{x}) = 0, \ \mathbf{x} \in \Re^d\}. \tag{2}$$

In this work, we define the scalar function $\varphi(\cdot)$ as the sum of K weighted RBFs:

$$\varphi(\mathbf{x}) = \sum_{i=1}^{K} T_i(\mathbf{x} - \mathbf{c}_i)\phi_s(\|\mathbf{x} - \mathbf{c}_i\|), \tag{3}$$

where $\|\cdot\|$ is the Euclidean norm and $T_i(\cdot)$ is a weighting function for the RBF $\phi_s(\cdot)$. The one-argument function $\phi_s : \Re_+ \to \Re$ is the RBF centered at $\mathbf{c}_i$, $\mathbf{c}_i \in \Re^d$. This work adopts the Wendland's ψ-functions, $\psi_{3,1}$, as the function ϕ_s because of its advantages of compact support property and low computational complexity (Wendland, 1995; Fornefett et al., 2001):

$$\phi_s(r) = \begin{cases} \left(1 - \dfrac{r}{s}\right)^4 \left(\dfrac{4r}{s} + 1\right), & 0 \leq r < s, \\ 0, & s \leq r, \end{cases} \tag{4}$$

where s is the shape parameter for accommodating various extents of the compact support. Given the outward normal vector $\mathbf{n}_i$ at $\mathbf{c}_i$, the weighting function $T_i : \Re^d \to \Re$ is defined as

$$T_i(\mathbf{v}) = \mathbf{v}^t \mathbf{n}_i. \tag{5}$$

Therefore, each $T_i(\cdot)\phi_s(\cdot)$ term in Eq. (3) implicitly represents a line as the zero set in 2D image space. The normal vector at the RBF center determines the orientation of the line and the summation of these products results in a smooth contour representation, as illustrated in Fig. 4. Notice that we only consider the zero set within the support extents of RBFs and usually the contour does not pass through RBF centers in this model. From the implicit function, the normal vector $\mathbf{n}_i$ at the control point $\mathbf{c}_i$ is calculated as

$$\mathbf{n}_i = \frac{\nabla \varphi(\mathbf{c}_i)}{\|\nabla \varphi(\mathbf{c}_i)\|}. \tag{6}$$

During the contour evolution, we adaptively allocate or deallocate RBFs according to the distance between the neighboring RBF centers.

2.4.2. Contour evolution forces

The brain area on each slice is determined by iteratively moving each RBF center $\mathbf{c}_i$ along the normal direction $\mathbf{n}_i$ to a compromise between an internal force $F_s(\mathbf{c}_i)$ and an external force $F_e(\mathbf{c}_i)$, $i = 1 \ldots K$:

$$\frac{\partial \mathbf{c}_i}{\partial t} = (aF_s(\mathbf{c}_i) + bF_e(\mathbf{c}_i)) \mathbf{n}_i, \tag{7}$$

where the weighting parameters a and b are both generally set to be 0.5.

The internal force calculated from the contour itself is used to keep the contour smooth during the evolution process. We define the smoothness constraint function $F_s(\cdot)$ at $\mathbf{c}_i$ as the averaged magnitude of the orientation differences between the normal vector $\mathbf{n}_i$ and the normal vectors $\mathbf{n}_{i-1}$ and $\mathbf{n}_{i+1}$ of $\mathbf{c}_i$'s neighboring RBFs centered at $\mathbf{c}_{i-1}$ and $\mathbf{c}_{i+1}$:

$$F_s(\mathbf{c}_i) = \mathbf{u}_i^t \mathbf{n}_i \times \frac{\|\mathbf{n}_i - \mathbf{n}_{i-1}\| + \|\mathbf{n}_i - \mathbf{n}_{i+1}\|}{2}, \tag{8}$$

where $\mathbf{u}_i$ is the normalized vector which starts from $\mathbf{c}_i$ and points to the midpoint between $\mathbf{c}_{i-1}$ and $\mathbf{c}_{i+1}$. Because each RBF keeps a distance to its neighboring ones, the contour smoothness is estimated from a larger scale of view, compared to the local curvature $\nabla \mathbf{n}_i$ estimated at $\mathbf{c}_i$.

The external force is used to evolve the initial contour toward its target boundary. Here we modify the external force adopted in Zhuang et al. (2006), which originated from Dale et al. (1999) and Smith (2002), as follows:

$$F_e(\mathbf{c}_i) = w(d, \alpha, s') \times \left(\frac{I_{\min}(\mathbf{c}_i)}{I_{\max}(\mathbf{c}_i)} - \beta\right). \tag{9}$$

The function above is designed according to the phenomenon that the intensity contrast between the CSF and GM/WM is usually high. Functions $I_{\min}(\cdot)$ and $I_{\max}(\cdot)$ find the local minimum intensity and local maximum intensity, respectively, among several sampled pixels starting from each RBF center $\mathbf{c}_i$ along the opposite direction of $\mathbf{n}_i$:

$$I_{\min}(\mathbf{c}_i) = \max(t_1, \min(t_m, I(\mathbf{c}_i), I(\mathbf{c}_i - \mathbf{n}_i),$$
$$I(\mathbf{c}_i - 2\mathbf{n}_i), \ldots, I(\mathbf{c}_i - M\mathbf{n}_i))), \tag{10}$$

$$I_{\max}(\mathbf{c}_i) = \min(t_2, \max(t_w, t_m, I(\mathbf{c}_i), I(\mathbf{c}_i - \mathbf{n}_i),$$
$$I(\mathbf{c}_i - 2\mathbf{n}_i), \ldots, I(\mathbf{c}_i - N\mathbf{n}_i))), \tag{11}$$
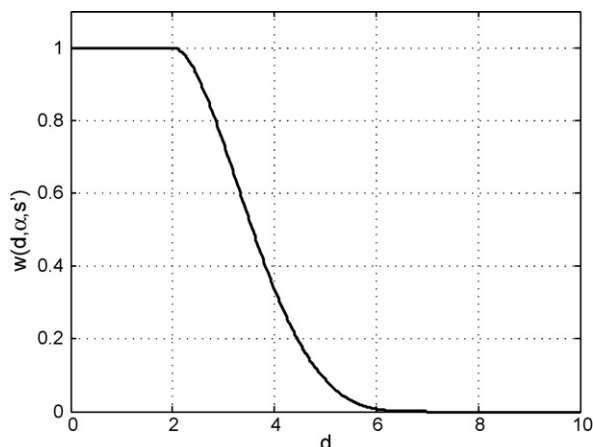
Fig. 5. The weighting function $w(d, \alpha, s')$ used to constrain the moving distance d of the RBF while evolving from its initial position. In this example, α and s' are set to be 2 and 5, respectively.

where M and N determine the search ranges and t_m is the median intensity of the brain tissues on each slice, which is approximated from the pixels within the initial brain region. The parameter β is used to characterize the intensity contrast between the brain and non-brain tissues. Its value is slightly larger than the intensity ratio of the CSF to WM:

$$\beta = \frac{t_c}{t_w} + k, \tag{12}$$

where k is a small positive number. In this way the value of the parameter β is not fixed but adaptively determined because the WM and CSF intensities, t_w and t_c, are estimated from the MR image. This advantage benefits the robustness of the proposed brain extraction method. Generally, the distance N in $I_{\max}(\cdot)$ should be large enough to reach the WM during the evolution. Therefore, $I_{\max}(\cdot)$ roughly equals to the local WM intensity. If the evolving contour is inside the brain region, $I_{\min}(\cdot)$ is most likely the intensity of GM or WM. This results in a positive external force and drives the contour outward. Once the contour is outside the brain boundary, $I_{\min}(\cdot)$ is most likely the CSF intensity and the resulted negative external force (approximately $-k$) pulls the contour inward.

Because the brain boundaries of neighboring slices are usually similar, we apply a weighting function $w(\cdot)$ to constrain the moving distance d of the RBF while the deformable model evolves from its initial position. Here the weighting function $w(\cdot)$ is defined as the Wendland's RBF in Eq. (4) with support extent s':

$$w(d, \alpha, s') = \phi_{s'}(\max(0, d - \alpha)). \tag{13}$$

As the example shown in Fig. 5, $w(\cdot)$ begins to gradually decrease to zero when the moving distance d is larger than α. Therefore, this function regularizes the amount of brain contour evolution and thus imposes the smoothness constraint of the extracted brain volume across adjacent slices. Note that this term is set to be the constant one in the extraction process for each of the starting slices.

2.5. Integration of segmentation results

The brain regions determined from the coronal and sagittal slices are complementary and thus can be integrated to increase the sensitivity of brain extraction. Segmentation results of the sagittal slices are first transformed back to the native space because these slices are sampled from the planes parallel to the detected MSP. Logical OR operation is then applied to combine the coronal and the transformed sagittal results. Finally, we apply morphological opening with a circle as the structural element to remove the weak connected components and to smooth the brain surface. Fig. 6 illustrates the extraction results of a T1-weighted head image.

2.6. Performance evaluation

This section introduces the methods used to evaluate the performance of the proposed brain extraction algorithm, including the data sets, performance criteria, and the approaches used for comparisons. The obtained accuracy evaluation results are further analyzed by two-sample t-test for performance comparison among the brain extraction methods. Moreover, previous evaluation works can be found in Lee et al. (2003), Boesen et al. (2004), and Fennema-Notestine et al. (2006).

2.6.1. Brain extraction algorithms for performance comparisons

The proposed method was compared with the Brain Surface Extractor (BSE) in BrainSuite2 (Sandor and Leahy, 1997; Shattuck et al., 2001; Shattuck and Leahy, 2002), Brain Extraction Tool (BET) version 2.1 (Smith et al., 2001; Smith, 2002), Hybrid Watershed Algorithm (HWA) version stable 3 (Ségonne et al., 2004), and Model-based Level Set (MLS) version 0.5 (Zhuang et al., 2006). The programs of the compared methods used in our experiments were downloaded from their webpages. BET, BSE, HWA, and our method were implemented in C++ whereas MLS was programmed in Java. All extraction experiments were performed on an AMD Opteron 240 processor running Linux, except BSE. Software of BSE is available only for Windows system, thus we evaluated its performance on another machine with an AMD XP 2400+ processor. Furthermore, we adopted the nearest neighbor sampling in our implementation because of not only its efficiency but also its accuracy compared to the trilinear interpolation. This observation agrees with the findings in Smith (2002). The reason could be that sampling methods other than the nearest neighbor somewhat blur images and the resulted weak boundaries may deteriorate the accuracy of brain extraction.

2.6.2. Image data sets with manual segmentation results

Two sets of T1-weighted head MR images as well as manual segmentation results were obtained from the Internet Brain Segmentation Repository (IBSR).[1] In the experiments, we applied extraction algorithms to determine the brain volumes of these subjects and employed the manually segmented brain areas, including the ventricles, to evaluate the extraction accuracy.

The first IBSR data set comprises 20 MR volumes, each with around 60 coronal slices, matrix size 256 mm × 256 mm, FOV 256 mm × 256 mm, and slice thickness 3.1 mm. Obvious intensity inhomogeneity and other significant artifacts present in most of the MR images in this data set. Another challenge of this data set is that the neck and even shoulder areas are included. This may influence the extraction accuracy of BET and HWA methods, as the examples shown in Figs. 7a and c (HWA even failed to process eighteen of the 20 MR images), because the excess non-brain tissues severely bias the estimation of the required parameters. To fairly evaluate extraction performance, several inferior slices of the image volumes containing neck or shoulder area were manually removed beforehand. In this way, BET and HWA achieved better segmentation results, as shown in Fig. 7b and d.

The second IBSR data set contains eighteen MR images, each with around 128 coronal slices, matrix size 256 mm × 256 mm, FOV 240 mm × 240 mm, and slice thickness 1.5 mm. All images were transformed to radiological convention beforehand based on the orientation information obtained from IBSR. These images have superior quality in contrast to those in the first data set. According to

---

[1] IBSR was developed by the Center for Morphometric Analysis at Massachusetts General Hospital and is available at http://www.cma.mgh.harvard.edu/ibsr.
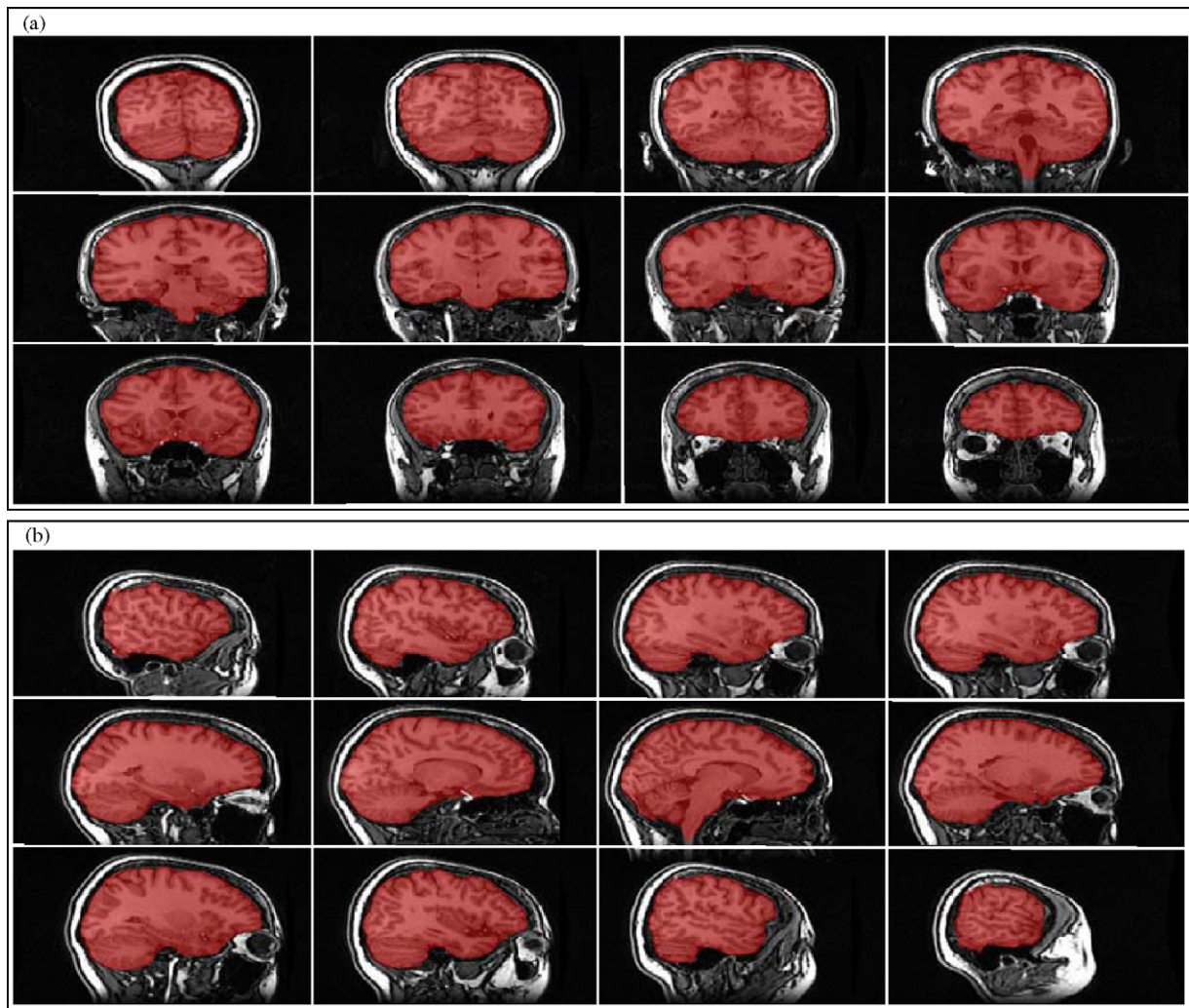
Fig. 6. Brain extraction results of a T1-weighted image shown in (a) coronal and (b) sagittal views.

the document of IBSR, each image in this data set has been roughly registered to the Talairach space and the intensity inhomogeneity has been corrected using the software developed by the Center for Morphometric Analysis at the Massachusetts General Hospital.

2.6.3. Criteria for extraction accuracy assessment

Several criteria are utilized to measure the extraction accuracy, including the Jaccard similarity coefficient (JSC), the sensitivity and specificity coefficients, and the risk evaluation of the segmentation results. The JSC, also known as the Jaccard index, is an extensively adopted measurement which evaluates the similarity between the extracted brain region B and the corresponding ground truth A:

$$JSC(A, B) = \frac{|A \cap B|}{|A \cup B|}, \tag{14}$$

where $|\cdot|$ denotes the cardinality value. The value of JSC is within [0, 1] and a larger JSC value means a better overlap with the ground truth.

Brain extraction is usually a compromise between the high recognizing percentage for brain voxels (that is, high sensitivity) and the high rejecting percentage for non-brain voxels (that is, high specificity). Therefore, the coefficients of sensitivity S_e and specificity S_p can be used to characterize brain extraction algorithms:

$$S_e = \frac{TP}{TP + FN}, \tag{15}$$

$$S_p = \frac{TN}{TN + FP}. \tag{16}$$

The true positive rate, TP, and false positive rate, FP, are the number of voxels correctly and incorrectly classified as brain tissues, respectively. The true negative rate, TN, and false negative rate, FN, are the number of voxels correctly and incorrectly classified as non-brain tissues, respectively.

In some applications, it is more important to avoid missing brain tissues than to reject all non-brain regions. From this point of view, Ségonne et al. (2004) proposed an error function E to measure the extraction risk:

$$E(c) = \frac{p_f + cp_m}{1 + c}, \tag{17}$$

where c is the risk ratio between the probabilities of missed detection for brain tissues, p_m, and false alarm, p_f. These two probabilities are calculated as

$$p_m = \frac{|A - B|}{|A \cup B|}, \tag{18}$$

$$p_f = \frac{|B - A|}{|A \cup B|}, \tag{19}$$

where B is the extracted brain region, A is the corresponding ground truth, and $|\cdot|$ denotes the cardinality value.
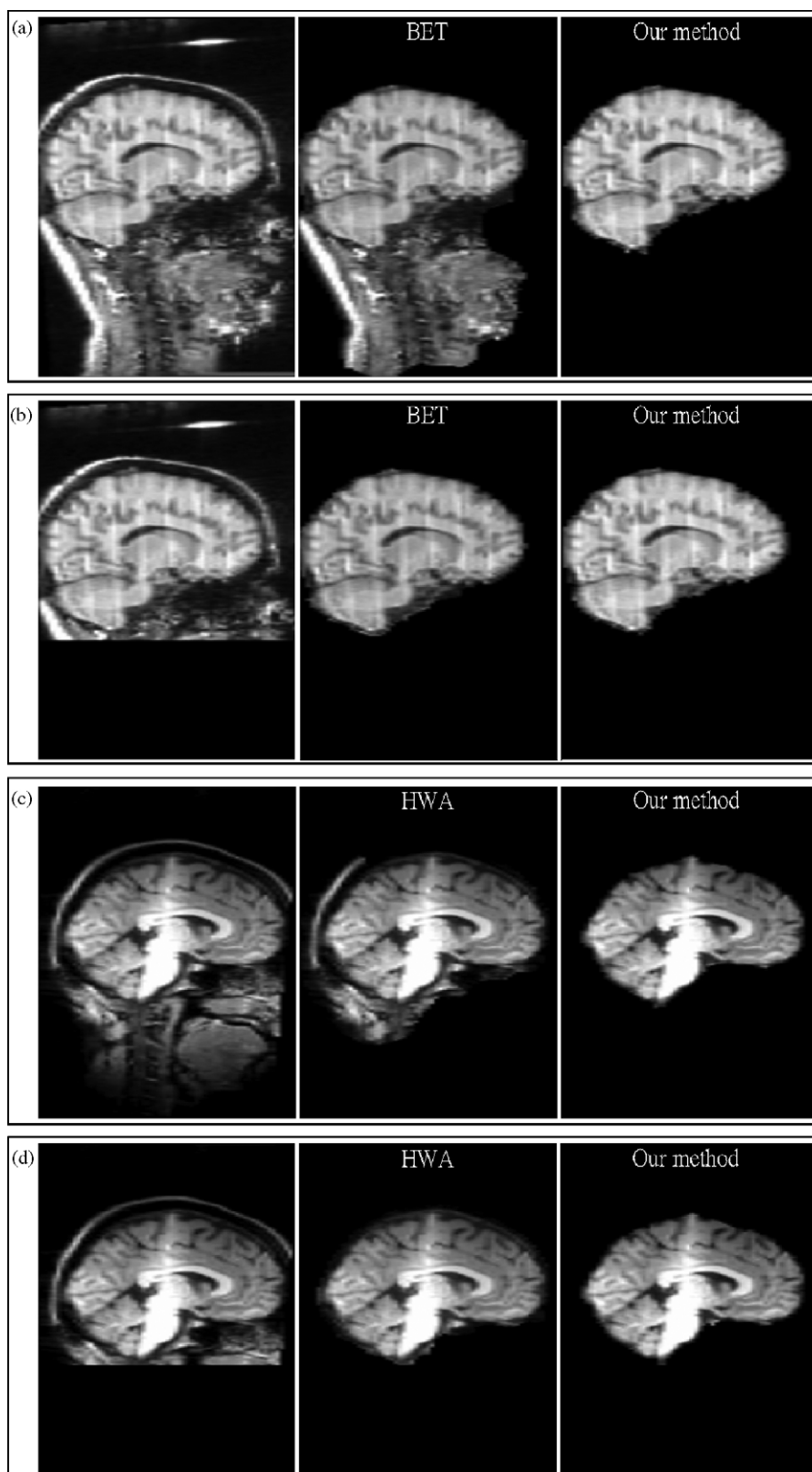
Fig. 7. Excess non-brain tissues affect the extraction accuracy of BET and HWA. The MR images of the first IBSR data set contain neck areas, as shown in the left of (a) and (c). In this case BET and HWA cannot well extract the brain volumes, as shown in the middle of (a) and (c). Manually removing several inferior non-brain slices, as shown in the left of (b) and (d), can facilitate BET and HWA to produce better extraction results, as shown in the middle of (b) and (d). On the other hand, the proposed method is relatively robust to the excess non-brain tissues, as shown in the right from (a) to (d).

2.6.4. Parameters of brain extraction algorithms

The parameters of the compared methods were determined to achieve the best average JSC value for each data set. In other words, there were two sets of parameter values for each method and each set is for one data set. For the first (second) IBSR image set, the smoothness weighting of MLS was chosen as 0.05 (0.1); the fractional intensity threshold of BET was set to be 0.6 (0.7); the parameters of HWA were set to the default values (default values with surface-shrink option turned on); the parameter k of the proposed method was set to be 0.15 (0.15); and the edge constant, diffusion iteration, and diffusion constant of BSE were set to be 3 (3), 1 (1), and 0.70 (0.66), respectively.

3. Experimental results

This section presents our results of performance evaluation for brain extraction methods. Table 1 lists the experimental outcomes of the proposed and other brain extraction algorithms using the first IBSR data set. In general, MLS and our method performed better than others. Jointly considering both the sensitivity and specificity, the accuracy indices of BET and BSE were moderate among the five methods evaluated. In this experiment, HWA did not achieve significant outperformance for all accuracy criteria ($p > 0.05$). Notice that the performance indices of each method shown in Table 1 did not count in the cases that (1) the JSC value between the extracted brain volume and the ground truth is smaller than 0.6 (three cases for BSE); (2) the program terminates without any results (three cases for HWA); and (3) the extraction result is blank (one case for BSE and one case for MLS). Excluding these cases (seven in total), all methods achieved slightly larger JSC values, which means better overlapping of the extracted brain regions with the ground truths, as shown in Table 2. HWA had remarkable improvement in its sensitivity due to the omission of additional four poor cases. Because of the exclusion of these seven cases, outperformance of BSE and MLS to our method became significant in terms of the specificity ($p = 0.001$) and JSC ($p = 0.024$), respectively.

To verify that the manual removal of slices containing neck or shoulder region in the first experiment did not largely affect the performance for BSE, MLS, and the proposed methods, we applied these three algorithms again to extract the brain volumes from original IBSR images. The obtained results indicated that these three algorithms produced similar extraction outcomes no matter the excess non-brain slices were removed or not.

Table 3 lists the experimental results of the proposed and other extraction algorithms using the second IBSR data set. Our method generally performed better than others with respect to all accuracy criteria, except for the sensitivity. HWA achieved the best sensitivity in detecting brain tissues at the expense of the relatively low specificity. BET, MLS, and BSE were statistically equal in all accuracy criteria, except for the specificity of BSE. BSE had the significantly lower specificity in detecting non-brain regions compared to BET ($p = 0.046$) and MLS ($p = 0.02$).

Tables 1–3 also list the average execution time of extraction methods using the first and second IBSR data sets. Both experiments show that BSE achieved the best efficiency, followed by BET and our method, though BSE was executed on a relatively low-end processor. The processing time of HWA and MLS was apparently longer among the compared methods. Notice that MLS has a chance to achieve better efficiency if the algorithm is implemented in C/C++, instead of Java.

For each brain extraction method, the probabilities of the false classification for brain and non-brain voxels, p_m and p_f, were calculated to evaluate its extraction risk. Fig. 8a shows the risk profiles of the first experiment when the risk ratio c between p_m and p_f ranged from 1 to 10. It is apparent that MLS and our method have relatively lower extraction risks. BET and HWA perform better than
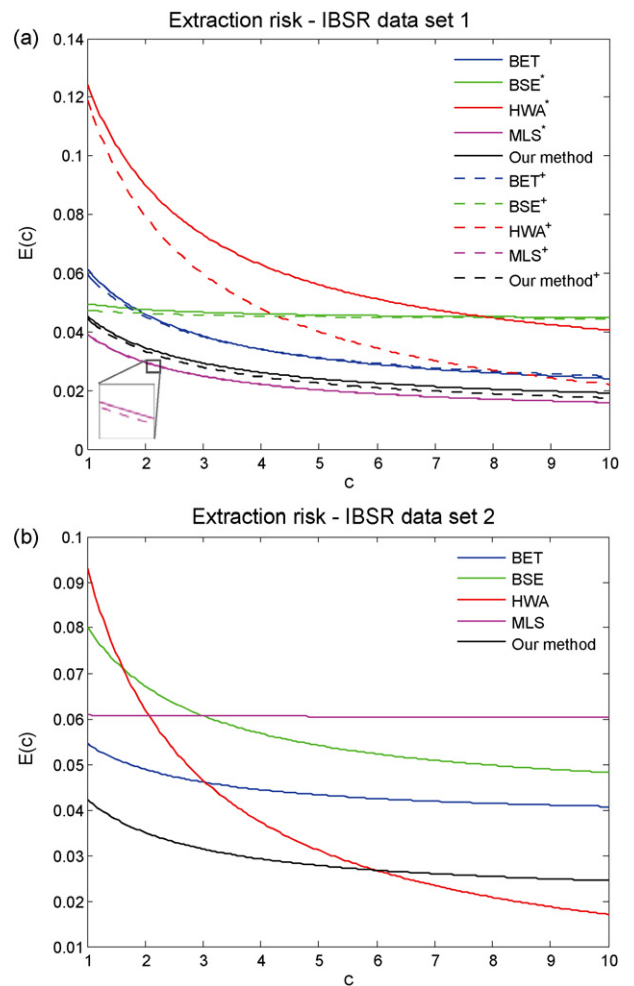

Fig. 8. Extraction risk evaluation using (a) the first IBSR data set and (b) the second IBSR data set. The mark "∗" indicates that some failed or extremely poor segmentation case(s) are not included. After excluding all of these cases for each method, the risk profiles are shown as the dashed lines in (a).

BSE when the risk ratio is larger than 1.8 and 8.0, respectively. This figure also illustrates the extraction risk for the results excluding the seven subjects that caused markedly poor results. We can see that the performance of the proposed method, BSE, and MLS has been slightly improved. The extraction risk of HWA decreases rapidly due to its high sensitivity to the inclusion of brain tissues. The risk profiles of the second experiment shown in Fig. 8b indicate that the proposed method has the lowest extraction risk compared to other algorithms if the penalty is smaller than 6. HWA performs better than BSE, MLS, BET, and our method if the risk ratio is larger than 1.6, 2.0, 3.0, and 6.0, respectively.

4. Discussion

Our method implicitly represents the brain contours with the proposed deformable model and explicitly evolves the contours by moving the RBF centers of the deformable model. Wendland's RBFs can well represent smooth object boundaries and are thus appropriate for brain extraction. By utilizing the explicit evolution, boundary determination of our method is efficient, at the expense of not being able to change the model topology. Therefore, the proposed model is appropriate for the application in which the object to be segmented has the same topology as the initial contour. Moreover, the performance of our deformable model, in terms of both accuracy and efficiency, can be further improved by considering

Table 1
Performance evaluation using the first IBSR data set after excluding the unsatisfactory results of each brain extraction algorithm.

Method	JSC	S_e	S_p	p_m	p_f	Time (s)
BET	0.878 (0.017)[A]	0.983 (0.023)	0.987 (0.004)[a]	0.016 (0.022)	0.107 (0.021)[A]	11.4 (0.8)[*]
BSE[4]	0.900 (0.025)	0.954 (0.035)[A]	0.993 (0.003)	0.044 (0.034)[A]	0.055 (0.017)[B]	3.6 (1.0)[+]
HWA[3]	0.752 (0.037)[A]	0.974 (0.068)	0.970 (0.008)[A]	0.022 (0.056)	0.226 (0.026)[A]	96.1 (24.7)[*]
MLS[1]	0.922 (0.025)	0.989 (0.010)	0.992 (0.006)	0.011 (0.009)	0.067 (0.031)	228.6 (28.0)[*]
Proposed method	0.910 (0.018)	0.986 (0.013)	0.991 (0.005)	0.013 (0.013)	0.077 (0.027)	14.4 (3.6)[*]

The superscripts in the first column indicate the number of the excluded cases. The marks "*" and "+" indicate that the experiments were executed on an AMD Opteron 240 processor running Linux and an AMD XP 2400+ processor running Windows XP, respectively. mean (standard deviation). A: the proposed method is superior to the compared method with $p < 0.01$. (a) The proposed method is superior to the compared method with $p < 0.05$. (B) The compared method is superior to the proposed method with $p < 0.01$.

Table 2
Performance evaluation using the first IBSR data set without considering all the cases which caused unsatisfactory results.

Method	JSC	S_e	S_p	p_m	p_f	Time (s)
BET[7]	0.881 (0.017)[A]	0.981 (0.026)	0.988 (0.003)[A]	0.017 (0.024)	0.102 (0.021)[A]	11.5 (0.9)[*]
BSE[7]	0.905 (0.025)	0.954 (0.035)[A]	0.994 (0.002)[B]	0.044 (0.034)[A]	0.051 (0.010)[B]	3.7 (1.0)[+]
HWA[7]	0.762 (0.012)[A]	0.999 (0.001)[b]	0.967 (0.008)[A]	0.001 (0.001)[b]	0.237 (0.013)[A]	91.6 (16.2)[*]
MLS[7]	0.922 (0.023)[b]	0.989 (0.010)	0.992 (0.006)	0.011 (0.010)	0.067 (0.030)[b]	230.2 (30.0)[*]
Proposed method[7]	0.911 (0.014)	0.988 (0.015)	0.991 (0.004)	0.012 (0.014)	0.077 (0.023)	19.9 (2.9)[*]

The superscripts in the first column indicate the number of the excluded cases. The marks "*" and "+" indicate that the experiments were executed on an AMD Opteron 240 processor running Linux and an AMD XP 2400+ processor running Windows XP, respectively. mean (standard deviation). (A) The proposed method is superior to the compared method with $p < 0.01$. (a) The proposed method is superior to the compared method with $p < 0.05$. (B) The compared method is superior to the proposed method with $p < 0.01$. (b) The compared method is superior to the proposed method with $p < 0.05$.

adaptive RBF placement. For example, sparsely (densely) deploying RBFs with larger (smaller) support extent to the boundary with smaller (larger) curvature.

The first experiment indicated that excess non-brain tissues may greatly affect the extraction accuracy of BET and HWA. Neck or shoulder region in the image volume largely biases the estimation of brain centroid and brain size. Therefore, BET may locate the initial surface far from a reasonable position and thus fail to drive it toward the target. For HWA, the deviation of initial parameters may cause erroneous estimation of tissue intensity in the following watershed procedure. On the contrary, the proposed method is more robust that the excess non-brain regions do not obviously affect the segmentation results, as the examples shown in Fig. 7. In this work, we considered fully automated procedure for brain extraction. Nevertheless, softwares of both BET and HWA provide options for the manual specification of brain radius and centroid parameters to remedy the biased estimation caused from the excess non-brain regions.

Three of the compared methods, BSE, HWA, and MLS, obtained unsatisfactory extraction results or even failed for some subject(s) in the first experiment. These cases were further analyzed to comprehend the underlying properties of these extraction algorithms. By correcting the intensity inhomogeneity beforehand using the N3 method (Sled et al., 1998), MLS produced good extraction result for the previously failed case whereas BSE and HWA still obtained unsatisfactory results. This suggests that inhomogeneity correction may improve the extraction stability of MLS. The failed cases of HWA resulted from program termination because the estimated brain size or WM intensity was too large. Manual specification of

brain centroid and radius can avoid the extraction failure of HWA. This suggests that poor image quality may cause poor initial extraction results for the watershed procedure, a thresholding/clustering method, of HWA. From the excluded cases of BSE, we observed that all the images present systematic edge artifacts caused by, for example, the noise spike in k-space. Enlarging the kernel size of diffusion smoothing, BSE can improve the extraction accuracy for the images with moderate edge artifacts though it could not tackle the images with obvious edges, as shown in Fig. 9. On the other hand, the proposed method and BET are more robust because these two methods did not obtain poor results for the first IBSR data set.

Images of the first IBSR data set are with relatively poor quality and manifest themselves in high intensity inhomogeneity, low signal-to-noise ratio, and other significant artifacts. Image quality of the second IBSR data set is closer to what a modern MR image scanner can achieve. Quantitative evaluation results shown in Tables 1–3 indicated that our method can accurately extract the brain volumes for the images in both sets, and this may imply that the proposed method is less sensitive to image quality compared to other algorithms. These experiments also show that the segmentation risk using HWA decreases rapidly as the relative importance to the inclusion of brain tissues increases. This phenomenon implies that HWA is appropriate if applications prefer to keep most brain voxels at the expense of the inclusion of non-brain tissues, such as the meninges and venous sinuses.

Quantitative morphometric studies of brain MR images require a large number of subjects to increase the statistical power. In this case, MR images used for structural analysis are probably obtained from different scanners (Schnack et al., 2004; Jovich et al., 2006).

Table 3
Performance evaluation for brain extraction algorithms using the second IBSR data set.

Method	JSC	S_e	S_p	p_m	p_f	Time (s)
BET	0.891 (0.052)[a]	0.959 (0.042)	0.989 (0.005)	0.038 (0.038)	0.071 (0.031)	17.9 (2.9)[*]
BSE	0.838 (0.083)[a]	0.957 (0.042)[a]	0.973 (0.030)[a]	0.041 (0.041)[a]	0.119 (0.104)	14.9 (0.5)[+]
HWA	0.814 (0.040)[A]	0.9997(0.0003)[B]	0.965 (0.016)[A]	0.0002 (0.0002)[B]	0.186 (0.040)[A]	101.5 (9.7)[*]
MLS	0.878 (0.081)[a]	0.938 (0.099)	0.989 (0.007)	0.060 (0.098)	0.061 (0.037)	485.8 (86.1)[*]
Proposed method	0.915 (0.018)	0.978 (0.011)	0.990 (0.003)	0.021 (0.011)	0.064 (0.022)	27.4 (1.9)[*]

The marks "*" and "+" indicate that the experiments were executed on an AMD Opteron 240 processor running Linux and an AMD XP 2400+ processor running Windows XP, respectively. mean (standard deviation). A: the proposed method is superior to the compared method with $p < 0.01$. (a) The proposed method is superior to the compared method with $p < 0.05$. (B) The compared method is superior to the proposed method with $p < 0.01$.
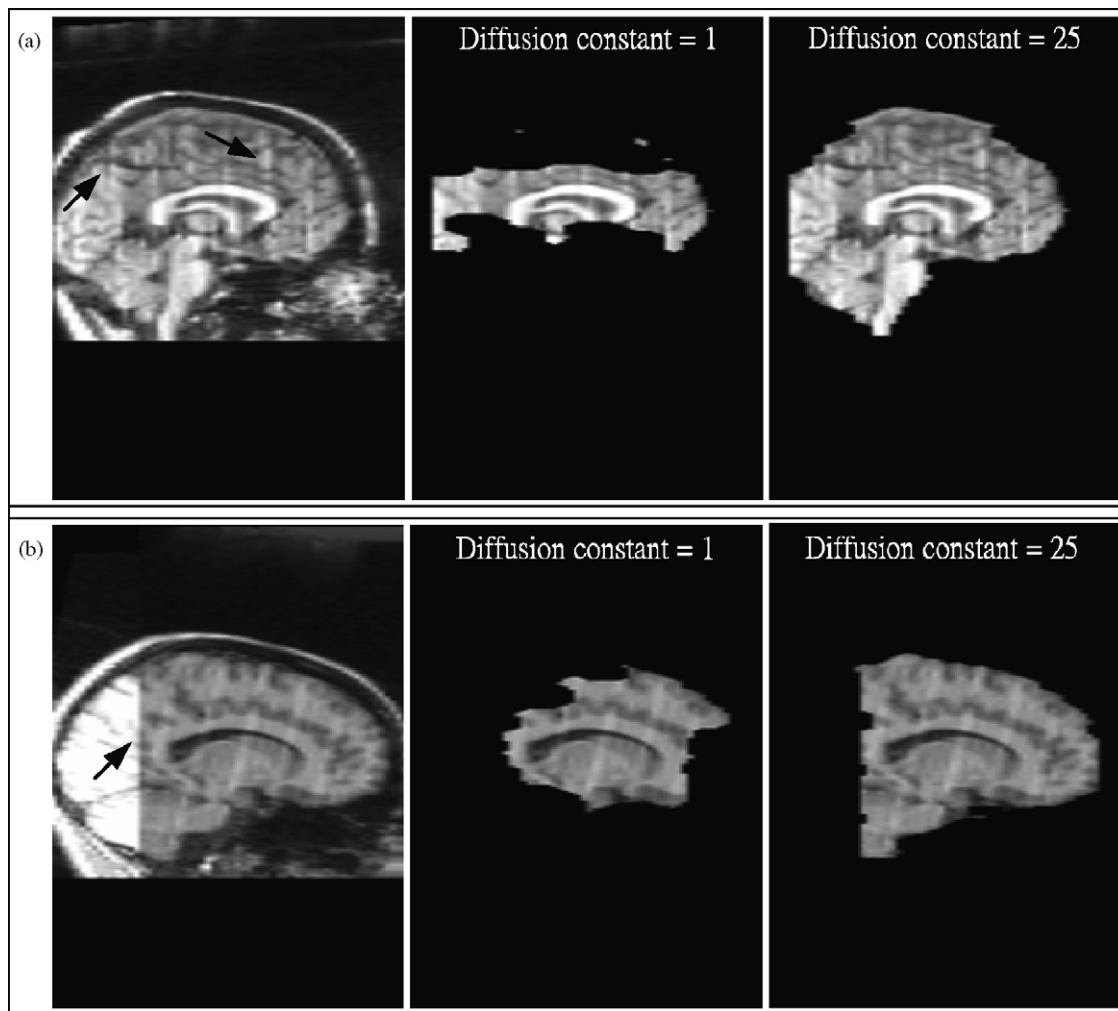
Fig. 9. Influence of systematic edge artifacts, indicated by the arrows, to the extraction results of BSE. (a) A large kernel size of diffusion smoothing may facilitate BSE to improve the brain extraction results for the images with moderate edge artifacts, (b) but not for the images with obvious edges.

Because the tissue intensity of multi-site images can vary considerably, a robust brain extraction algorithm should prevent from the parameter adjustment for images obtained by different scanners. To accommodate the various intensity properties, we utilize DOG to estimate the principal parameter of our algorithm, the intensity ratio of CSF to WM. The use of image derivative reduces the influence of noise and intensity inhomogeneity. Thresholded DOG can robustly reveal the regions with relatively low and high intensity and thus it provides good information for the estimation of global CSF and WM intensities.

In conclusion, we have proposed an implicit deformable model and developed a novel brain extraction method for head MR images. Experimental results using two IBSR data sets indicated that our method can extract brain volumes with high accuracy compared to four existing algorithms, which have been extensively applied in neuroimaging applications.

References

Aboutanos GB, Nikanne J, Watkins N, Dawant BM. Model creation and deformation for the automatic segmentation of the brain in MR images. IEEE Trans Biomed Eng 1999;46:1346–56.

Acosta-Cabronero J, Williams GB, Pereira JMS, Pengas G, Nestor PJ. The impact of skull-stripping and radio-frequency bins correction on grey-matter segmentation for voxel-based morphometry. NeuroImage 2008;39: 1654–65.

Ashburner J, Friston KJ. Voxel-based morphometry—the methods. NeuroImage 2000;11:805–21.

Atkins MS, Mackiewich BT. Fully automatic segmentation of the brain in MRI. IEEE Trans Med Imaging 1998;17:98–107.

Baillard C, Hellier P, Barillot C. Segmentation of brain 3D MR images using level sets and dense registration. Med Image Anal 2001;5:185–94.

Beyer JL, Krishnan KRR. Volumetric brain imaging findings in mood disorders. Bipolar Disord 2002;4:89–104.

Boesen K, Rehm K, Schaper K, Stoltzner S, Woods R, Luders E, et al. Quantitative comparison of four brain extraction algorithms. NeuroImage 2004;22:1255–61.

Bomans M, Höhne KH, Tiede U, Riemer M. 3-D segmentation of MR images of the head for 3-D display. IEEE Trans Med Imaging 1990;9:177–83.

Brenneis C, Bösch SM, Schocke M, Wenning GK, Poewe W. Atrophy pattern in SCA2 determined by voxel-based morphometry. NeuroReport 2003;14:1799–802.

Brummer ME, Mersereau RM, Eisner RL, Lewine RRJ. Automatic detection of brain contours in MRI data sets. IEEE Trans Med Imaging 1993;12:153–66.

Cox RW. AFNI: Software for analysis and visualization of functional magnetic resonance neuroimages. Comput Biomed Res 1996;29:162–73.

Dale AM, Fischl B, Sereno MI. Cortical surface-based analysis—I. Segmentation and surface reconstruction. NeuroImage 1999;9:179–94.

Davatzikos C, Bryan RN. Using a deformable surface model to obtain a shape representation of the cortex. IEEE Trans Med Imaging 1996;15:785–95.

Fein G, Landman B, Tran H, Barakos J, Moon K, Di Sclafani V, et al. Statistical parametric mapping of brain morphology: sensitivity is dramatically increased by using brain-extracted images as inputs. NeuroImage 2006;30:1187–95.

Fennema-Notestine C, Ozyurt IB, Clark CP, Morris S, Bischoff-Grethe A, Bondi MW, et al. Quantitative evaluation of automated skull-stripping methods applied to contemporary and legacy images: effects of diagnosis, bias correction, and slice location. Hum Brain Mapp 2006;27:99–113.

Fornefett M, Rohr K, Stiehl HS. Radial basis functions with compact support for elastic registration of medical images. Image Vis Comput 2001;19:87–96.

Germond L, Dojat M, Taylor C, Garbay C. A cooperative framework for segmentation of MRI brain scans. Artif Intell Med 2000;20:77–93.

Gholipour A, Kehtarnavaz N, Briggs R, Devous M, Gopinath K. Brain functional localization: a survey of image registration techniques. IEEE Trans Med Imaging 2007;26:427–51.

Good CD, Johnsrude I, Ashburner J, Henson RNA, Friston KJ, Frackowiak RSJ. Cerebral asymmetry and the effects of sex and handedness on brain structure: a voxel-based morphometric analysis of 465 normal adult human brains. NeuroImage 2001a;14:685–700.

Good CD, Johnsrude IS, Ashburner J, Henson RNA, Friston KJ, Frackowiak RSJ. A voxel-based morphometric study of ageing in 465 normal adult human brains. NeuroImage 2001b;14:21–36.

Hahn HK, Peitgen HO. The skull stripping problem in MRI solved by a single 3D watershed transform. Lect Notes Comput Sci 2000;1935:134–43.

Hata Y, Kobashi S, Hirano S, Kitagaki H, Mori E. Automated segmentation of human brain MR images aided by fuzzy information granulation and fuzzy inference. IEEE Trans Syst Man Cybern C: Appl Rev 2000;30:381–95.

Huh S, Ketter TA, Sohn KH, Lee CH. Automated cerebrum segmentation from three-dimensional sagittal brain MR images. Comput Biol Med 2002;32:311–28.

Jenkinson M, Smith S. A global optimisation method for robust affine registration of brain images. Med Image Anal 2001;5:143–56.

Jovicich J, Czanner S, Greve D, Haley E, van der Kouwe A, Gollub R, et al. Reliability in multi-site structural MRI studies: effects of gradient non-linearity correction on phantom and human data. NeuroImage 2006;30:436–43.

Karas GB, Burton EJ, Rombouts SARB, van Schijndel RA, O'Brien JT, Scheltens P, et al. A comprehensive study of gray matter loss in patients with Alzheimer's disease using optimized voxel-based morphometry. NeuroImage 2003;18:895–907.

Kelemen A, Székely G, Gerig G. Elastic model-based segmentation of 3-D neuroradiological data sets. IEEE Trans Med Imaging 1999;18:828–39.

Lee C, Huh S, Ketter TA, Unser M. Unsupervised connectivity-based thresholding segmentation of midsagittal brain MR images. Comput Biol Med 1998;28:309–38.

Lee JM, Yoon U, Nam SH, Kim JH, Kim IY, Kim SI. Evaluation of automated and semi-automated skull-stripping algorithms using similarity index and segmentation error. Comput Biol Med 2003;33:495–507.

Lemieux L, Hagemann G, Krakow K, Woermann FG. Fast, accurate, and reproducible automatic segmentation of the brain in T1-weighted volume MRI data. Magn Reson Med 1999;42:127–34.

Liu JX, Chen YS, Chen LF. Affine and nonlinear spatial normalization techniques using derivatives of brain magnetic resonance images. In: Proceedings of the 14th annual meeting of the organization for human brain mapping; 2008a.

Liu JX, Chen YS, Chen LF. Nonlinear registration based on the approximation of radial basis function coefficients. J Med Biol Eng 2008b;28:119–26.

Mikheev A, Nevsky G, Govindan S, Grossman R, Rusinek H. Fully automatic segmentation of the brain from T1-weighted MRI using Bridge Burner algorithm. J Magn Reson Imaging 1999;27:1235–41.

Montagnat J, Delingette H, Ayache N. A review of deformable surfaces: topology, geometry and deformation. Image Vis Comput 2001;19:1023–40.

Otsu N. Threshold Selection Method from Gray-Level Histograms. IEEE Trans Syst Man Cybern 1979;9:62–6.

Rehm K, Schaper K, Anderson J, Woods R, Stoltzner S, Rottenberg D. Putting our heads together: a consensus approach to brain/non-brain segmentation in T1-weighted MR volumes. NeuroImage 2004;22:1262–70.

Rex DE, Shattuck DW, Woods RP, Narr KL, Luders E, Rehm K, et al. A meta-algorithm for brain extraction in MRI. NeuroImage 2004;23:625–37.

Sandor S, Leahy R. Surface-based labeling of cortical anatomy using a deformable atlas. IEEE Trans Med Imaging 1997;16:41–54.

Schnack HG, van Haren NEM, Pol HEH, Picchioni M, Weisbrod M, Sauer H, et al. Reliability of brain volumes from multicenter MRI acquisition: a calibration study. Hum Brain Mapp 2004;22:312–20.

Ségonne F, Dale AM, Busa E, Glessner M, Salat D, Hahn HK, et al. A hybrid approach to the skull stripping problem in MRI. NeuroImage 2004;22:1060–75.

Shattuck DW, Leahy RM. BrainSuite: An automated cortical surface identification tool. Med Image Anal 2002;6:129–42.

Shattuck DW, Sandor-Leahy SR, Schaper KA, Rottenberg DA, Leahy RM. Magnetic resonance image tissue classification using a partial volume model. NeuroImage 2001;13:856–76.

Sled JG, Zijdenbos AP, Evans AC. A nonparametric method for automatic correction of intensity nonuniformity in MRI data. IEEE Trans Med Imaging 1998;17:87–97.

Smith S, Bannister PR, Beckmann C, Brady M, Clare S, Flitney D, et al. FSL: new tools for functional and structural brain image analysis. NeuroImage 2001;13:249.

Smith SM. Fast robust automated brain extraction. Hum Brain Mapp 2002;17:143–55.

Stokking R, Vincken KL, Viergever MA. Automatic morphology-based brain segmentation (MBRASE) from MRI-T1 data. NeuroImage 2000;12:726–38.

Ward BD. Intracranial segmentation. Technical report. Medical College of Wisconsin; 1999.

Wendland H. Piecewise polynomial, positive definite and compactly supported radial functions of minimal degree. Adv Comput Math 1995;4:389–96.

Woods RP, Grafton ST, Watson JDG, Sicotte NL, Mazziotta JC. Automated image registration: II. Intersubject validation of linear and nonlinear models. J Comput Assist Tomogr 1998;22:153–65.

Worth AJ, Makris N, Meyer JW, Caviness VS, Kennedy DN. Semiautomatic segmentation of brain exterior in magnetic resonance images driven by empirical procedures and anatomical knowledge. Med Image Anal 1998;2:315–24.

Xu C, Pham DL, Prince JL. Image segmentation using deformable models. In: Fitzpatrick JM, Sonka M, editors. Handbook of medical imaging. Bellingham, WA: SPIE Press; 2000. p. 129–74.

Zhang YY, Brady M, Smith S. Segmentation of brain MR images through a hidden Markov random field model and the expectation–maximization algorithm. IEEE Trans Med Imaging 2001;20:45–57.

Zhuang AH, Valentino DJ, Toga AW. Skull-stripping magnetic resonance brain images using a model-based level set. NeuroImage 2006;32:79–92.